



Efficient CO₂ reduction MOFs derivatives transformation mechanism revealed by *in-situ* liquid phase TEM

Liangping Xiao^a, Guanghua Wang^a, Xingchen Huang^a, Shiyuan Zhou^a, Rusen Zhou^a,
Youhong Jiang^a, Sangui Liu^a, Gen Li^a, Haimei Zheng^b, Shi-Gang Sun^a, Hong-Gang Liao^{a,*}

^a State Key Laboratory of Physical Chemistry of Solid Surfaces, Innovation Laboratory for Sciences and Technologies of Energy Materials of Fujian Province (IKKEM), College of Chemistry and Chemical Engineering, Xiamen University, Xiamen 361005, PR China

^b Materials Sciences Division, Lawrence Berkeley National Laboratory, Berkeley, CA 94720, USA

ARTICLE INFO

Keywords:

in-situ liquid phase TEM
Transformation mechanism
MOFs-based derivative
CO₂ reduction reaction

ABSTRACT

Materials derived from MOFs have great potentials in energy conversion. However, the nanoscale transformation processes of MOFs derivatives remain unknown. Herein, by using *in-situ* liquid phase TEM, we directly visualize the MOFs etching processes. For the first time, unexpected nanobubble stability controlled transformation mechanism of ZIF-67 to porous or layered cobalt transition metal hydroxide (Co-TMH) is identified. Voids in MOFs migrate and merge to form nanobubbles due to structural collapse. Under slow diffusion conditions, nanobubbles move slowly and Co-TMH clusters generate on the nanobubble interface, further favoring the formation of internal nanocages and porous structures. On the other hand, a fast diffusion leads to rapid nanobubbles generation, aggregation and reshaping, inducing layered structure formation. Inspired by *in-situ* observation, we further synthesize porous Co-TMH at – 80 °C under inhibited diffusion conditions, which exhibits excellent catalytic performance on CO₂ reduction reaction.

1. Introduction

The metal-organic frameworks (MOFs) derived materials have attracted much attention in energy conversion applications [1–3]. The inherent advantages in the nanocatalysts are indispensable, such as the increased density of active sites, efficient transfer reactants/products and enhanced accessibility of active surface sites [4–6]. The intrinsic activity of catalytic sites in the nanocatalysts can be tuned during the formation of MOFs-based materials [7]. Exploring the formation mechanism of various nanostructures is, therefore, a key precondition to obtaining desired catalysts. The transformation mechanisms of MOFs-based derivatives have been explored in the time gradient experiments [8]. Some believe that hydroxide nucleation sites depend on the hydrolysis rate of nitrates. For example, nanosheet derivatives instead of porous ones are synthesized in aqueous solutions due to the fast hydrolysis [9,10]. Controlling the balance between shell precipitation and template etching has been proved crucial to design the porous derivatives [11]. The protons generated from the hydrolysis will etch the MOFs templates, thus formatting hydroxide derivatives in the shells [12, 13]. Others suggest that the diffusion rate is another key factor during

the transformation process. Diffusion is a general process involving the motion of adsorbed atoms, molecules or clusters on the surface of solid materials [14–16]. Different diffusion rates between reactants and products will affect the structure of derivatives.

Understanding the MOFs based derivatives transformation mechanisms is a prerequisite for better controlling and tuning the structure of thus-obtained materials. However, many details regarding this transformation are controversial or even missing. The experimental evidence showing molecular-scale dynamics, therefore, is of urgent need. In recent years, significant developments in liquid phase transmission electron microscopy (TEM) have been made, allowing real-time imaging of the reaction process at high spatial and temporal resolution in a liquid environment [17–20]. By employing *in-situ* liquid phase TEM, the formation mechanisms of metal-organic nanotubes and metal-organic frameworks (UiO-66 and ZIF-8) have been investigated [21–24]. Nevertheless, real-time investigations on the transformation from MOFs to derivatives have rarely been reported. *In-situ* liquid phase TEM provides the opportunity to reveal the unknown details during the transformation, including etching, growth and diffusion, especially at nano-scale [25–27].

* Corresponding author.

E-mail address: hgliao@xmu.edu.cn (H.-G. Liao).

<https://doi.org/10.1016/j.apcatb.2022.121164>

Received 23 September 2021; Received in revised form 15 January 2022; Accepted 29 January 2022

Available online 1 February 2022

0926-3373/© 2022 Elsevier B.V. All rights reserved.

MOFs-based (such as ZIF-67) derivatives, including transition metal hydroxide (TMH), have been utilized and developed for energy conversion *via* electrocatalytic routes [28–31]. Cobalt-based nanocatalysts derived from MOFs exhibit outstanding catalytic activity, high product selectivity and durable catalytic stability on carbon dioxide reduction reaction (CO₂RR) [32–37]. These nanocatalysts are regarded as one of the most attractive alternatives for noble metals-based CO₂RR nanocatalysts, especially due to their lower cost and lower adsorption energy [38–41]. It is urgent to explore the formation process of nanostructures in cobalt MOFs-based TMH, which inevitably affects the performance of CO₂RR.

Herein, using *in-situ* liquid phase TEM, the transformation from ZIF-67 to porous and layered cobalt transition metal hydroxide (Co-TMH) is explored to reveal the nanoscale dynamics. In the beginning, voids in MOFs migrate and merge to form nanobubbles due to structural collapse. Under a slow diffusion condition, limited reaction reagent supply induces slow generation of metastable nanobubbles in MOFs. That induces Co-TMH clusters formation on the bubbles interface, leading to nanocages formation inside MOFs. Later, plenty of nanocages and porous structure are thus obtained. Under a faster diffusion condition, rigorous nanobubbles generation and rapid nanobubbles coalescence result in growth of Co-TMH nanosheets. Based on the *in-situ* observation and Stokes-Einstein equation [42], we successfully synthesize porous Co-TMH at – 80 °C under relatively unfavorable diffusion conditions. After electrochemical reduction treatment, the prepared electrocatalysts show excellent CO₂RR activity, selectivity and stability due to the porous structure and outstanding CO₂ adsorption capacities.

2. Experimental

2.1. Materials

Cobalt nitrate hexahydrate (Co(NO₃)₂·6H₂O) and 2-methylimidazole (2-MeIm) were purchased from Alfa Aesar. Methanol (CH₃OH) and ethanol (C₂H₅OH) were acquired from Xilong Chemical Co., Ltd. Potassium bicarbonate (KHCO₃, 99.99%) was purchased from Sigma-Aldrich. All chemicals were directly used without further purification. Ultrapure water (18.2 MΩ·cm) was produced by a Millibubble system. Hydrogen (H₂, 99.99%), argon (Ar, 99.999%), compressed air (extra dry), and carbon dioxide (CO₂, 99.999%) were purchased from Linde Group. The Nafion N-117 membrane with 0.18 mm thickness was purchased from Alfa Aesar.

2.2. Materials synthesis

2.2.1. Synthesis of ZIF-67 nanocrystals

ZIF-67 nanocrystals were synthesized as previous reports [8,12]. 498 mg Co(NO₃)₂·6H₂O was dissolved in 50 mL CH₃OH, and 656 mg 2-MeIm was added to 50 mL CH₃OH. At room temperature, the two solutions were mixed and then stirred for 24 h. Finally, the purple precipitates were washed with ethanol for 3 times through centrifugation before vacuum dried at 60 °C for 8 h.

2.2.2. Synthesis of hollow Co-TMH

100 mg Co(NO₃)₂·6H₂O was dissolved in 25 mL ethanol. 50 mg ZIF-67 nanocrystals were added to the solution and stirred for 2 h. The hollow Co-TMH was obtained, washed with ethanol and ultrapure water, and dried in vacuum oven at 60 °C for 8 h.

2.2.3. Synthesis of porous Co-TMH

50 mg ZIF-67 nanocrystals were dissolved in 25 mL ethanol by ultrasonication. 100 mg Co(NO₃)₂·6H₂O was dissolved in 25 mL ethanol before being added to the ZIF-67 dispersed solution and stored at – 80 °C without stirring. After washing with ethanol and water, the green precipitates were collected by centrifugation and vacuum dried overnight.

2.2.4. Synthesis of Co@porous Co-TMH

The porous Co-TMH was dissolved in ethanol. The slurry was dropped on the carbon cloth and dried at room temperature before serving as the working electrode. A platinum foil and a Ag/AgCl electrode were applied as the counter electrode the reference electrode, respectively. For the transformation of porous Co-TMH to Co@porous Co-TMH, the working electrode was biased at – 1.0 V for 1 h in 0.1 M KHCO₃ electrolyte. The resultant working electrode was immediately taken out of the electrolyte and briefly rinsed with deionized water.

2.2.5. Synthesis of Co@hollow Co-TMH

The Co@hollow Co-TMH was obtained as described above and used the hollow Co-TMH as the source material.

2.3. In-situ TEM imaging process

The liquid cells with a 10 nm thick SiN_x window and TEM holder were customized from CHIP-NOVA [17–20]. The liquid cells and holders were shown in Fig. S1a–S1f. To observe the transformation of ZIF-67 to porous Co-TMH, the raw ZIF-67 was sonochemically dispersed into fragments and then injected into liquid cells. About 50 nL Co (NO₃)₂·6H₂O solution (4 mg mL^{–1}, in Ar-saturated ethanol) was injected into the liquid cells. Later, the liquid cells were sealed with epoxy and dried out. As a control, the transformation process from ZIF-67 to Co-TMH nanosheets was tracked in liquid cells under a faster diffusion condition. The ZIF-67 fragments were first dropped onto the liquid cell chips and assembled with the upper chip by assembling equipment (Fig. S1g), containing a thicker liquid layer with a thick spacer. Finally, the Co(NO₃)₂·6 H₂O solution was injected into the liquid cells and the cells were sealed with epoxy. To prevent solvents from affecting the vacuum of electron microscopy, leakage inspections of liquid cells and flow cells were performed using a CHIP-NOVA leak detector (Fig. S1h), before the holder with the liquid cell was loaded into the TEM for *in-situ* observations. TEM images were carried out in FEI F20 and Talos with an acceleration voltage of 200 kV. High-resolution TEM (HRTEM) images, high angle annular dark-field scanning transmission electron microscopy (HAADF-STEM) and the elemental mapping were conducted using a ThermoFisher Talos operated at 200 kV. A beam current density of about 6 e[–]/(Å²·s) was used within the whole observation. A high sensitivity TVIPS CMOS camera was used for real-time imaging at low dose conditions, which allowed a time resolution of 300 frames per second.

2.4. Characterizations

The crystal structure was characterized by X-ray diffraction (XRD) using a Bruker-axs (Cu Kα X-ray source, 40 kV and 40 mA). The Brunauer-Emmett-Teller (BET) and Barrett-Joyner-Halenda (BJH) were applied to detect the specific surface area and bubble size distribution using a TriStar II Plus. The amount of adsorbed CO₂ was measured on a TriStar II physisorption analyzer.

2.5. Electrochemical measurements

The electrochemical measurements were carried out at an electrochemical workstation (CHI660C) with a custom-designed gas-tight H-type electrochemical cell separated with a Nafion-117 proton exchange membrane. 1 mg porous Co-TMH nanocatalysts were dispersed in 180 μL ethanol with 20 μL of 0.5 wt% Nafion, and sonicated to form a homogenous catalyst ink. The ink was drop-cast onto a 1 × 1 cm² pre-treated carbon cloth (HCP020P, from HESEN) and naturally dried. The catalysts area loading of 1 mg·cm^{–2} was obtained. The catalysts loaded carbon cloth was used as the working electrode and was placed in the cathodic compartment. A Pt gauze was applied as the counter electrode and was placed in the anodic compartment. Meanwhile, a Ag/AgCl electrode was used as the reference electrode and was placed in the cathodic compartment. The 30 mL KHCO₃ electrolyte with the

concentration of 0.1 mol·mL⁻¹ (0.1 M) was filled in the compartments of the cell. All potentials were converted to the reversible hydrogen electrode scale (RHE, $E_{\text{RHE}} = E_{\text{Ag/AgCl}} + 0.21 \text{ V} + 0.059 \text{ V} \times \text{pH}$). For the CO₂RR electrocatalysis on Co@porous Co-TMH, the carbon cloth loaded Co@porous Co-TMH catalysts was used as the working electrode and a flow rate of 20 mL·min⁻¹ of CO₂ was continuously bubbled into the cathode compartment. The electrochemical CO₂ electrolysis was performed in the CO₂-saturated 0.1 M KHCO₃ solution for 1 h at various electrolysis potentials between -0.5 V and -1.2 V. The linear sweep voltammetry (LSV) was carried out at a scan rate of 50 mV·s⁻¹.

2.6. Product analysis

The liquid and gaseous products were collected to evaluate the reactivity and the conversation Faradaic efficiency on the catalysts. The liquid products were quantified via nuclear magnetic resonance (NMR, Agilent 500 MHz) spectroscopy after being mixed with 100 μL D₂O containing 0.1% phenol (internal standard). The H₂O peak was suppressed by the suppression method. The concentration of formate (HCOO⁻) was quantified based on its NMR peak area, which was proportional to that of the internal standard using the calibration curve from a series of standard HCOONa solutions (Fig. S2). The representative ¹H NMR spectra of the liquid products obtained at different potentials were shown in Fig. S3. As shown in Fig. S4, the gaseous products were periodically injected into the gas-sampling loop of a gas chromatograph (GC, Agilent 880 C) every 7 min for 1 h of reaction and evaluated by the integral area ratio of the reduction products to standards. The Faradaic efficiency (FE) of liquid products was quantified by using the following equation [31,32]:

$$\text{FE} = (\text{CHCOO}^- \times V \times e \times N_A) / Q \quad (1)$$

where CHCOO^- represents the concentration of HCOO⁻ in the electrolyte after the electrolysis. V is the volume of the electrolyte. N_A and e represent the Avogadro's constant and the number of transferred electrons, respectively. And Q is the total electricity passed during the electrolysis reaction.

The Faradaic efficiency of gaseous products was evaluated via the following equation:

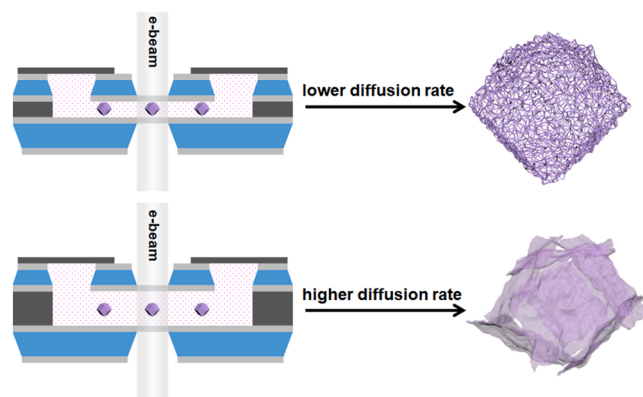
$$\text{FE} = (v \times X_{\text{H}_2 \text{ or CO}} \times e \times F) / j \quad (2)$$

where v is the flow rate of 20 mL·min⁻¹ of CO₂. X is the measured concentration of CO or H₂ based on the calibration of the GC with a standard gas. F and e represent the Faraday's constant and the number of transferred electrons, respectively. And j is the recorded current.

3. Results and discussion

3.1. Transformation mechanism of catalyst

In liquid cells, materials are embedded in thin liquid films, thus the diffusion behavior is substantially suppressed. The averaged diffusion coefficient of nanoparticles and reactants is much smaller than the reported values at the normal conditions [43,44]. The diffusion rates are quantified in liquid cells with different liquid layer thicknesses (Fig. S5) via the mean square displacement (MSD) of nanoparticles in the liquid cells from Brownian motion. The diffusion coefficient (D) is calculated based on the equation $\text{MSD} = 4Dt$ and a linear fit of the plot in Fig. S5 [18,43]. The average diffusion coefficient is 0.10 nm²/s in thin liquid cells (0.08, 0.09, 0.10, 0.11 and 0.12, respectively), while 3.1 nm²/s in thick liquid cells (2.93, 3.29, 3.10, 3.03 and 3.22, respectively). The lower diffusion coefficient is similar to the reported diffusion coefficient of nanoparticle in thin liquid cells [42,43]. Therefore, to further explore the role of diffusion during the transformation, liquid cells with different thicknesses of liquid layers are designed. The schematic (Scheme 1) illustrates the transformation of porous Co-TMH and Co-TMH nanosheets



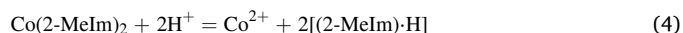
Scheme 1. The transformation from ZIF-67 to porous Co-TMH or layered Co-TMH under different liquid cell thicknesses observed by *in-situ* liquid phase TEM.

under both lower and faster diffusion conditions. The diffusion of reactants in liquid cells with about 100 nm thin liquid layer would be greatly suppressed, resulting in the porous structure of Co-TMH. On the contrary, the diffusion of reactants in the thicker ones is faster, leading to the formation of Co-TMH nanosheets.

In a typical experiment, the ZIF-67 was pretreated by ultrasonication to obtain nanosize fragments before being loaded into liquid cells, as shown in Fig. S6. Fig. 1b and Movie S1 visualize the etching and transformation of single MOF particle to porous Co-TMH by real-time TEM imaging. In the early stages, the small voids are randomly generated in the ZIF-67 nanoparticle (Fig. 1b at 1.8 s). Then, the aggregation and coalescence of voids induce the formation of larger nanobubbles (Fig. 1c). This phenomenon is commonly observed during the formation of porous nanomaterials [45]. Some nanobubbles gradually grow in the way of Ostwald ripening (Fig. 1e). In the end, the porous Co-TMH is obtained (Fig. 1b at 443.6 s). According to the statistics of nanobubbles of different sizes during the porous Co-TMH formation, the formation and disappearance of nanobubbles coexist, resulting in aggregation and coalescence as marked by red circles (Fig. 1i).

Supplementary material related to this article can be found online at doi:10.1016/j.apcatb.2022.121164.

The transformation between ZIF-67 nanoparticles and cobalt nitrate has been reported in the previous literature as following reaction [8–10]:



The protons generated from the hydrolysis of Co²⁺ ions capture 2-MeIm, break the coordinate, and then etch ZIF-67. Nanobubbles are formatted by the 2-MeIm diffusion into solution and the collapse of the initial structure. If the 2-MeIm is replaced by hydroxyl from the hydrolysis, the formation of Co-TMH occurs. As reported in relevant published studies, the large interfacial energy at the gas-solid interface leads to the formation of Co-TMH on the nanobubbles surface [46,47]. The contour changes of a nanobubble are recorded in Fig. 1f. The deformed circular structure is attributed to the influence of surrounding molecules and the formation of TMH clusters on the bubble surface. Under the inhibited diffusion condition, nanobubbles are relatively stable and move slowly, inducing more Co-TMH clusters formation on the gas-solid interface. As the reaction proceeds, the connection of Co-TMH clusters form nanocages around the surface of nanobubbles. Later, the porous Co-TMH consisting of plenty of Co-TMH nanocages inside is obtained. The scheme of the transformation process under the lower diffusion is shown in Fig. 1a. The Co-TMH clusters are red circled in Fig. 1g at 90.4 s, and the Co-TMH nanocage is highlighted by the red ring in Fig. 1g at 360.6 s

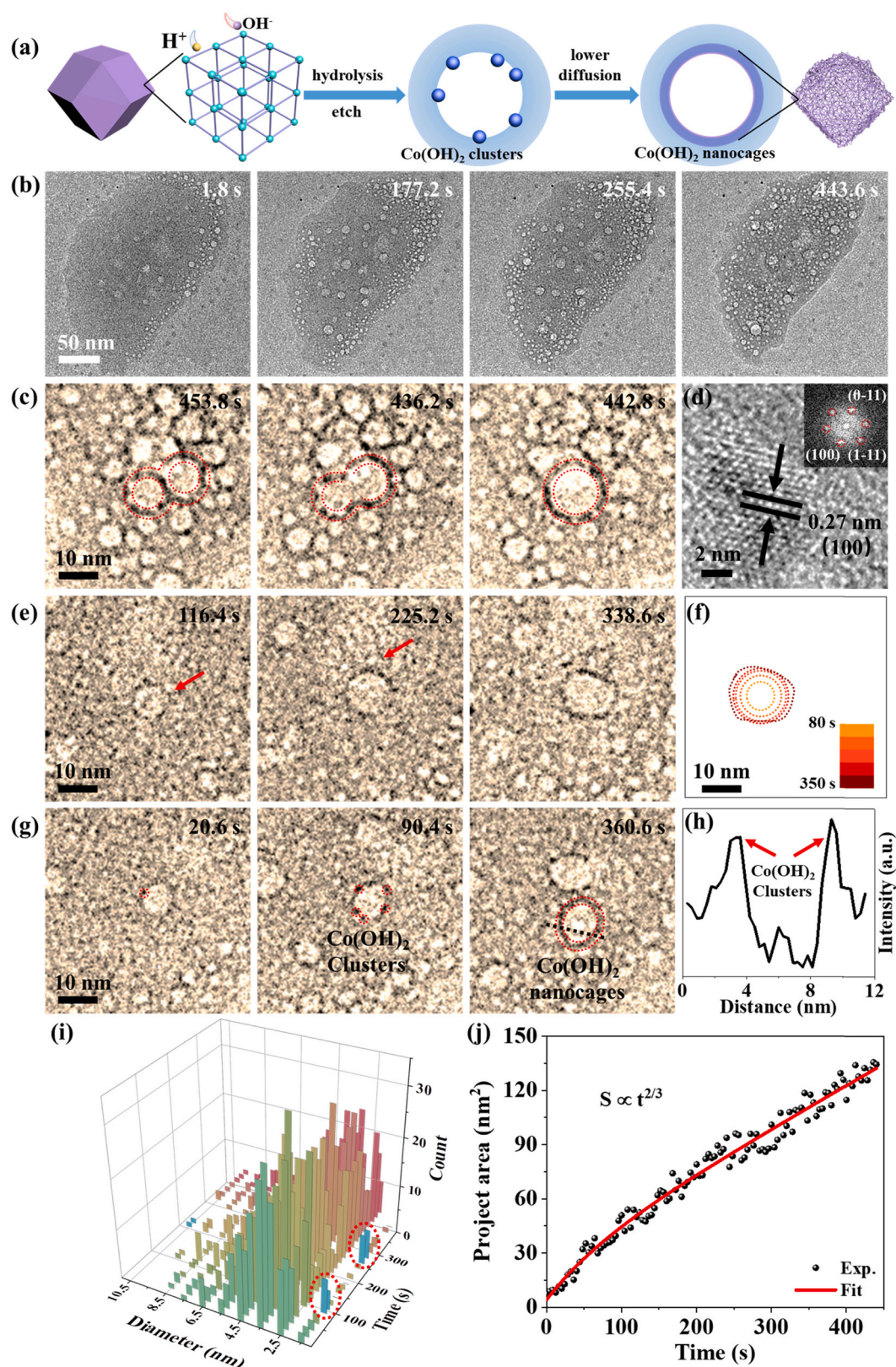


Fig. 1. (a) Scheme of MOFs based porous Co-TMH transformation process under the lower diffusion condition. (b) Sequential TEM images tracking the transformation process from ZIF-67 to porous Co-TMH. (c) Coalescence and (e) growth of smaller nanobubbles. (d) HRTEM image of the obtained porous Co-TMH and corresponding FFT inset. (f) Contour line of nanobubble evolution in (e). (g) Formation of Co-TMH clusters and nanocage around the nanobubble surface. (h) Strong contrast changes of the Co-TMH nanocage structure. (i) The size distribution of nanobubbles counted during porous Co-TMH formation. (j) The project area of nanobubbles changing as a function of time.

Thus-obtained porous Co-TMH shows lattice fringes of 0.27 nm corresponding to the space of (100) plane of $\text{Co}(\text{OH})_2$ in Fig. 1d [48]. The fast Fourier transformed (FFT, inset photograph) pattern matches the $\text{Co}(\text{OH})_2$ crystal. As shown in Fig. 1h, the Co-TMH clusters around the nanobubble surface inside ZIF-67 is confirmed by the dramatic change in contrast. TEM image contrast of Co-TMH cluster consists of mass-thickness contrast, which is approximately proportional to total number of atoms. The intensity values along the black line in Fig. 1g at 360.6 s demonstrate the changes of “dark-to-bright-to-dark”, marked by

the red arrows, attributed to the Co-TMH nanocage inside ZIF-67 [24, 49]. As for the growth kinetics, the formation of Co-TMH nanocage observed in the experiment follows the diffusion-limited growth as defined by the Lifshitz-Slyozov-Wagner (LSW) model. The power-law fit yields a growth exponent $t^{2/3}$ in Fig. 1j and Fig. S7 [22,50]. The results indicate that the stable nanobubbles induced Co-TMH nanocage formation is a diffusion-limited process, in which the diffusion of reactants and voids determines the rate-limiting step.

Experiments are also conducted under a faster diffusion condition

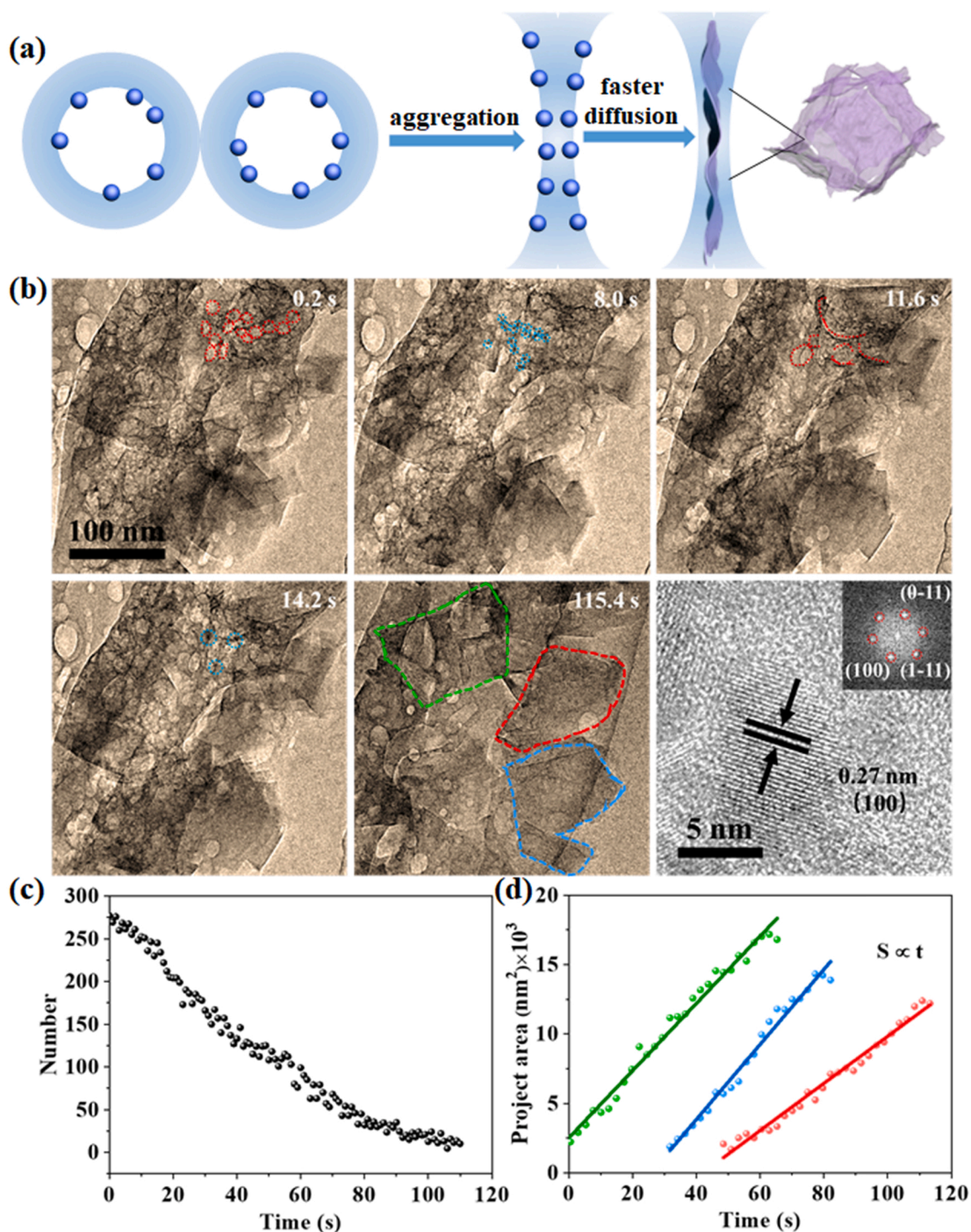


Fig. 2. (a) Scheme of MOFs based Co-TMH nanosheets transformation process under faster diffusion condition. (b) Sequential TEM images tracking the transformation from ZIF-67 to Co-TMH nanosheets, Co-TMH clusters and nanobubbles marked by red rings and blue rings, respectively. HRTEM image of the obtained Co-TMH nanosheets and corresponding FFT inset. (c) The numbers of nanobubbles counted during the Co-TMH nanosheets formation. (d) The project area of three Co-TMH nanosheets.

with a thicker reactants liquid layer of around 2 μm measured by TEM defocus. The formation of Co-TMH nanosheets is observed in the thicker liquid layer with a faster diffusion rate (Fig. 2 and Movie S2). Red rings at 0.2 s mark nanobubbles in the early stage (Fig. 2b). Under the fast diffusion condition, the nanobubbles move freely and merge quickly. TEM image at 11.6 s shows aggregated nanobubbles and some blurred bubble boundaries. At 8.0 s, the Co-TMH clusters are formed around the nanobubble surfaces, as marked by blue rings. With the aggregation of nanobubbles, Co-TMH rapidly aggregates and becomes larger to form the initial crystal nucleus of the layer Co-TMH (blue rings) at 14.2 s. Concurrently, the Co-TMH nanosheets continue to expand and grow in solution, as marked by different curves at 115.4 s. To confirm the universality of this phenomenon under the faster diffusion condition, another repeated *in-situ* investigation is conducted. As shown in Fig. S8 and Movie S3, the Co-TMH clusters are formatted on the surface of nanobubbles (marked at 1.8 s by red rings), and merge rapidly with the aggregation of nanobubbles (marked at 8.0 s), before developing into the Co-TMH nanosheets (marked at 11.6 s). As shown in Fig. 2a, the rapid coalescence of nanobubbles leads to fast aggregation of Co-TMH clusters on nanobubbles surface and induces growth of Co-TMH nanosheets. The number of nanobubbles decreases as nanosheets structure is formed due to the coalescence of nanobubbles (Fig. 2c). The project areas of different nanosheets are counted from Movie S2 in Fig. 2d. The power-law fit yields a growth exponent t , which indicates a reaction-limited growth here as defined by the LSW model [22,50]. The fringes in the HRTEM image of nanosheets is 0.27 nm, which corresponds to the plane (100) of $\text{Co}(\text{OH})_2$ [48]. Furthermore, investigations with the flow cells are also conducted to further verify the diffusion effect. To achieve higher flow rates, flow cells with wide gaps were employed. Although the thickness of the flow cell limited the details observed, it can also be clearly found that ZIF-67 nanocrystals are directly converted into hollow derivatives in Fig. S9 and Movie S4. These structures are formatted from nanosheets.

Supplementary material related to this article can be found online at [doi:10.1016/j.apcatb.2022.121164](https://doi.org/10.1016/j.apcatb.2022.121164).

In comparison with the formation of porous Co-TMH and Co-TMH nanosheets via *in-situ* experiments, we find an interesting interactive influence between bubble movement and Co-TMH precursor diffusion and crystallization. The initial nanobubbles are formed due to the 2-MeIm diffusion into solution and the collapse of the initial structure. Diffusion rate directly affects the migration of nanobubbles, which is positively correlated with movement of nanobubbles. If the nanobubbles move slowly, the small Co-TMH clusters nucleate on the bubble surface and coalesce to form a shell, thus stabilize the bubble. Yet, if the nanobubbles move rigorously and merge quickly, strong turbulence will lead to Co-TMH nanosheets formation. The growth kinetics is very different. During the formation of porous Co-TMH, diffusion is the limited step. Nevertheless, the rate-limiting step for the Co-TMH nanosheets formation is the surface reaction. The in-particle nanoscale diffusion and phase segregation greatly influence mass transfer and materials structure evolution kinetics.

A controlled experiment is carried out to explore the effect of the electron beam on the formation of porous Co-TMH. As shown in Fig. S10 and Movie S5, a small number of nanobubbles appear in ZIF-67 (39.0 s). When the beam is blocked, still, there are many nanobubbles (413.0 s), indicating the reaction still processing without being exposed to the electron beam. The transformation reaction from ZIF-67 to porous Co-TMH proceeds spontaneously, and the electron beam has no obvious effect on the transformation process at a low dose condition.

Supplementary material related to this article can be found online at [doi:10.1016/j.apcatb.2022.121164](https://doi.org/10.1016/j.apcatb.2022.121164).

3.2. Ex-situ synthesis of catalyst based on in-situ TEM experiments

The *in-situ* liquid phase TEM results show that restricted diffusion during the transformation reaction is crucial for forming porous

structures. Therefore, the rational design and controllable preparation of porous nanocatalysts are achievable through the precise regulation of the diffusion coefficient, defined by the following Stokes-Einstein equation [42,51–53]:

$$D = k_B T / 6\pi\mu r \quad (5)$$

where k_B is Boltzmann's constant, T is temperature, μ is the solution viscosity and r represents the radius. The diffusion coefficient is positively proportional to temperature and inversely proportional to the solution viscosity. From the Stokes-Einstein Eq. (5), it is obvious that the diffusion coefficient decreases with T/μ . The solution viscosity is also inversely proportional to temperature from the Antoine equation [54, 55]:

$$\log\mu = A + B/(T + C) \quad (6)$$

where A , B and C are the empirical constants related to the chemical composition. In ethanol solution, μ is calculated to ~ 1.1 mPa·s at ambient temperature, but to ~ 19.0 mPa·s at -80°C . Combining Eqs. (5) and (6), we obtain that the diffusion coefficient is closely related to temperature. For the transformation of ZIF-67 to Co-TMH in the ethanol solution, the diffusion coefficient decreases by 26 times at -80°C .

The strategy has been extended to design MOF-based porous Co-TMH by lowering the temperature and inhibiting diffusion. As shown in Fig. 3a, the schematic illustrates the transformation from ZIF-67 to porous Co-TMH at -80°C , and then electrochemical reduction to form a highly efficient CO_2RR electrocatalyst. As a control experiment, the hollow Co-TMH is obtained at ambient temperature, constructed by plenty of nanosheets in Fig. 3b. The HRTEM image reveals the lattice fringes with distances of 0.27 nm, corresponding to the (100) plane of the $\text{Co}(\text{OH})_2$ crystal structure. Nevertheless, the transformation from ZIF-67 to Co-TMH is different due to the difference of diffusion coefficients for ambient temperature and -80°C (Fig. S11a–S11f). The Co-TMH with porous structure is obtained at -80°C , revealed in TEM and HAADF-STEM images (Fig. 3c). The lattice distance of 0.27 nm is still ascribed to the (100) plane of $\text{Co}(\text{OH})_2$. After electrochemical reduction, the Co@porous Co-TMH remains the initial porous structure, as confirmed by TEM and STEM images (Fig. 3d). Meanwhile, the cobalt nanoparticles could be found, and the lattice fringes with distances of 0.22 nm corresponding to the Co (100) plane. O (red) and Co (green) elements are uniformly decorating in the whole hollow Co-TMH, porous Co-TMH and Co@porous Co-TMH. The XRD diffraction peaks also suggest the successful transformation from ZIF-67 to porous Co-TMH at -80°C and Co@porous Co-TMH in Fig. S12. The porous structures of Co-TMH and Co@porous Co-TMH give respectively large surface areas up to $440\text{ m}^2\cdot\text{g}^{-1}$ and $493\text{ m}^2\cdot\text{g}^{-1}$ (Fig. S13), which is larger than that of hollow Co-TMH obtained at ambient temperature, $127\text{ m}^2\cdot\text{g}^{-1}$. The reduced surface area of hollow Co-TMH could be ascribed to the coalescence and consumption of the nanobubbles during the transformation. Besides, the volumetric CO_2 adsorption capacities for hollow Co-TMH, porous Co-TMH and Co@porous Co-TMH are $30.18\text{ cm}^3\cdot\text{g}^{-1}$, $80.24\text{ cm}^3\cdot\text{g}^{-1}$ and $95.99\text{ cm}^3\cdot\text{g}^{-1}$ at 273 K, respectively (Fig. S14).

3.3. CO_2 reduction reaction performance of catalyst

The CO_2RR electrocatalytic performance of Co@porous Co-TMH is evaluated in a membrane-separated two-compartment cell in a CO_2 -saturated 0.1 M KHCO_3 solution. The polarization curve shows a cathodic current onset at approximately -0.6 V versus RHE, and then quickly increases to about $-38.0\text{ mA}\cdot\text{cm}^{-2}$ at -1.2 V (Fig. 4a). Furthermore, to analyze and quantify the CO_2RR products, the electrochemical CO_2 electrolysis is performed between -0.5 V and -1.2 V for one hour. Formate is the primary CO_2RR product, together with a trace amount of CO. The formate FE stably maintains over 90% in a wide negative potential range from -0.7 V to -1 V (Fig. 4b). Compared with Co@porous Co-TMH, the Co@hollow Co-TMH displays poor CO_2RR

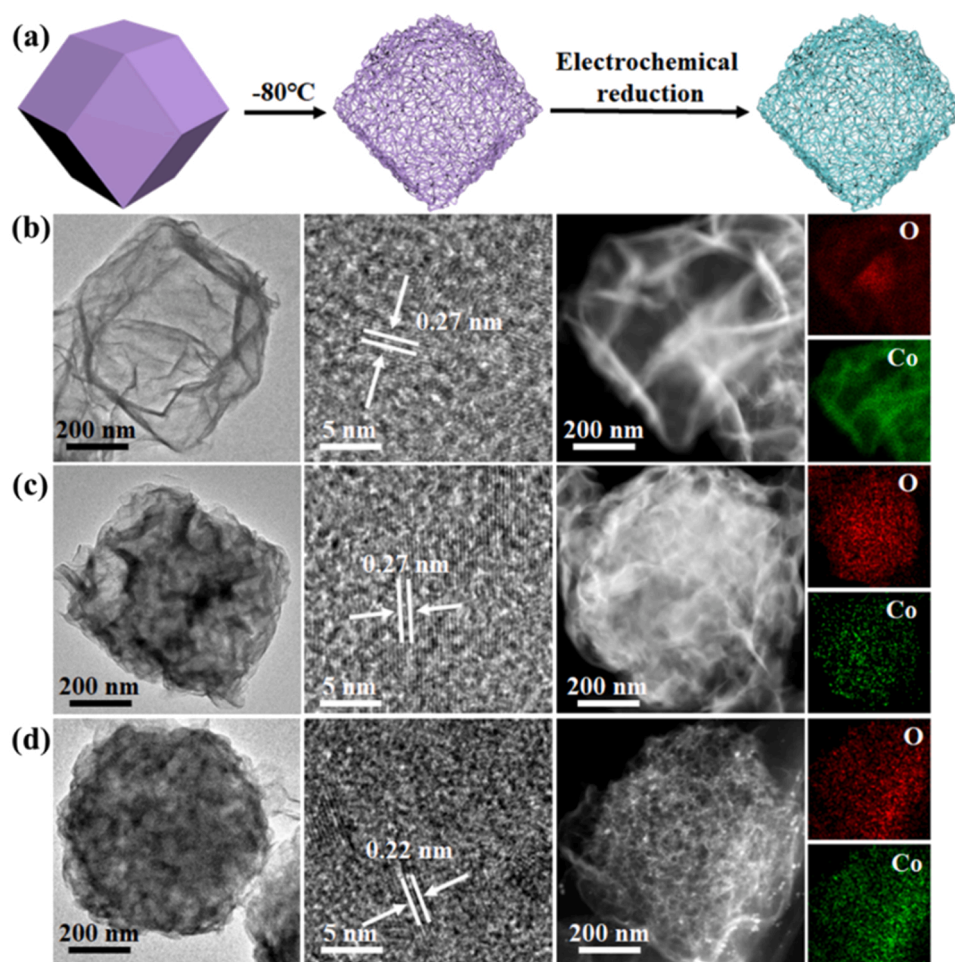


Fig. 3. (a) Schematic illustration of the transformation process from ZIF-67 to porous Co-TMH and Co@porous Co-TMH. TEM, HRTEM images and element mappings of (b) hollow Co-TMH, (c) porous Co-TMH and (d) Co@porous Co-TMH.

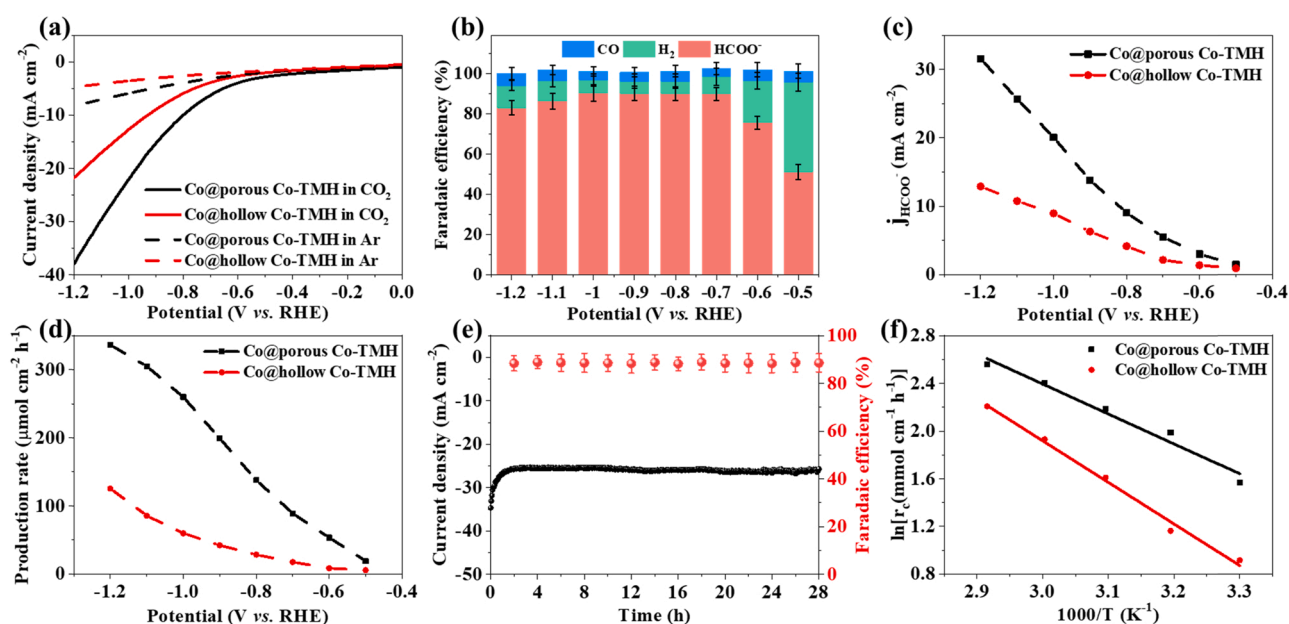


Fig. 4. (a) LSV curves of Co@porous Co-TMH and Co@hollow Co-TMH in CO_2 -saturated or Ar-saturated 0.1 M KHCO_3 electrolyte. (b) The Faradaic efficiencies of formate, H_2 and CO on Co@porous Co-TMH. (c) The partial current density of formate and (d) formate production rate on Co@porous Co-TMH and Co@hollow Co-TMH. (e) The long-term electrolysis experiments on Co@porous Co-TMH at the electrolysis potential of -1 V . (f) The apparent activation energy for CO_2RR on Co@porous Co-TMH and Co@hollow Co-TMH.

performances, exhibiting the onset potential of -0.7 V and a cathodic current density of approximately -21.8 mA·cm $^{-2}$. The FE for formate on Co@hollow Co-TMH reaches about 70% only between -0.8 V and -1 V (Fig. S15). Additionally, the formate partial current density is plotted against the working potential for Co@porous Co-TMH and Co@hollow Co-TMH (Fig. 4c). The Co@porous Co-TMH exhibits a large j_{HCOO^-} of 31.6 mA·cm $^{-2}$ at -1.2 V, which is about 2.5-times higher than Co@hollow Co-TMH (12.9 mA·cm $^{-2}$). Meanwhile, the formate production rate of Co@porous Co-TMH (336.4 $\mu\text{mol}\cdot\text{cm}^{-2}\cdot\text{h}^{-1}$) is much larger than that of Co@hollow Co-TMH (125.7 $\mu\text{mol}\cdot\text{cm}^{-2}\cdot\text{h}^{-1}$) (Fig. 4d). The Co@porous Co-TMH also demonstrates outstanding stability over 28 h without significant performance decay at -1 V. The current density maintains at around -20 mA·cm $^{-2}$ with the FE of formate being approximately 90% (Fig. 4e). Moreover, the morphology, crystal structure and the comparison of the composition of Co@porous Co-TMH before and after 28 h electrolysis show negligible changes on the STEM image, XRD patterns and XPS spectra (Fig. S16), demonstrating the excellent durability of the Co@porous Co-TMH catalyst. The initial one-electron transfer to form the adsorbed CO_2^* for the catalysts has been studied by the Tafel slope. The Co@porous Co-TMH has a much lower Tafel slope of 124 mV·dec $^{-1}$ than Co@hollow Co-TMH (195 mV·dec $^{-1}$) (Fig. S17), indicating that faster initial electron transfer on the Co@porous Co-TMH surface. To further assess the CO_2 RR activity, the activation energy (E_a) for Co@porous Co-TMH and Co@hollow Co-TMH has been calculated. As shown in Fig. 4f, the E_a for Co@porous Co-TMH and Co@hollow Co-TMH is 30.2 kJ·mol $^{-1}$ and 41.9 kJ·mol $^{-1}$, respectively. The porous structure of Co@porous Co-TMH has great influence on substrate adsorption, desorption and diffusion, which affect both reaction rate and selectivity. In addition, the reactive sites at the edges of porous Co@porous Co-TMH possess unsaturated coordination sites as well as dangling bonds, which decrease the activation energy barrier and enable the stabilization of the reaction intermediates, as suggested in the literatures [56–59]. They provide a path with a lower activation energy compared to the uncatalyzed reactions, thus increasing the reaction rate constant. The lower activation energy indicates the low activation barrier for the key step and CO_2 activation is achieved on Co@porous Co-TMH because of the higher density of the exposed sites in the porous structure.

4. Conclusions

In summary, we visualize the transformation of ZIF-67 to porous or layered Co-TMH via *in-situ* liquid phase TEM. Under slow diffusion conditions, accompany with the etching of ZIF-67 and replacement of 2-MeIm by hydroxyl, the voids in MOFs migrate and aggregate to form nanobubbles. The metastable nanobubbles in MOFs facilitate the Co-TMH clusters formation on the bubble interface, thus generating abundant nanocages inside, which further leads to the porous structure formation. The growth kinetics of porous Co-TMH reveals a diffusion-limited process defined by the LSW model, in which the transportation of reactants is the rate-limiting step. At faster diffusion conditions, voids and nanobubbles undergo rapid aggregation and coalescence, leading to the growth of Co-TMH nanosheets. Guided by the *in-situ* liquid phase TEM results, porous Co-TMH is successfully prepared by limiting the diffusion rate at -80 °C. The Co@porous Co-TMH demonstrates excellent catalytic activity, selectivity and stability in CO_2 RR due to the unique porous structure and outstanding CO_2 adsorption capacities. This work unveils unexpected bubble stability controlled transformation mechanisms of MOFs-based materials providing a new perspective on catalysts synthesis.

CRedit authorship contribution statement

Liangping Xiao: Conceptualization, Methodology, Resources, Validation, Investigation, Writing – original draft. **Guanghua Wang:** Data Curation, Validation, Formal analysis, Visualization. **Xingchen Huang:**

Investigation, Methodology, Data curation. **Shiyuan Zhou:** Conceptualization, Visualization, Investigation. **Rusen Zhou:** Conceptualization, Methodology, Writing – review & editing. **Youhong Jiang:** Investigation, Methodology, Visualization. **Sangui Liu:** Visualization, Validation, Writing – review & editing. **Gen Li:** Conceptualization, Writing – review & editing. **Haimei Zheng:** Resources, Supervision, Writing – review & editing. **Shi-Gang Sun:** Supervision, Funding acquisition, Writing – review & editing. **Hong-Gang Liao:** Conceptualization, Supervision, Writing – review & editing, Project administration.

Declaration of Competing Interest

The authors declare that they have no known competing financial interests or personal relationships that could have appeared to influence the work reported in this paper.

Acknowledgements

This work was financially supported by the National Natural Science Foundation of China (Grant Nos. 91934303, 21991151, 21991150 and 21673198) and the National Key Research and Development Program of China (2017YFA0206500).

Appendix A. Supporting information

Supplementary data associated with this article can be found in the online version at doi:10.1016/j.apcatb.2022.121164.

References

- [1] D. Saliba, M. Ammar, M. Rammal, M. Al-Ghoul, M. Hmadeh, Crystal growth of ZIF-8, ZIF-67, and their mixed-metal derivatives, *J. Am. Chem. Soc.* 140 (2018) 1812–1823.
- [2] L.H. Zhang, J.F. Chen, W.T. Huang, Y.Y. Hu, J.H. Cheng, Y.C. Chen, Preparations and electrocatalytic properties of Cu-bipy-BTC-derived carbon-based catalyst for oxygen reduction reaction, *J. Electrochem.* 25 (2019) 511–521.
- [3] G. Yilmaz, S.B. Peh, D. Zhao, G.W. Ho, Atomic- and molecular-level design of functional metal-organic frameworks (MOFs) and derivatives for energy and environmental applications, *Adv. Sci.* 6 (2019), 1901129.
- [4] L. Wu, Y. Li, Z.Y. Fu, B.L. Su, Hierarchically structured porous materials: synthesis strategies and applications in energy storage, *Nat. Sci. Rev.* 7 (2020) 1667–1701.
- [5] M.H. Sun, S.Z. Huang, L.H. Chen, Y. Li, X.Y. Yang, Z.Y. Yuan, B.L. Su, Applications of hierarchically structured porous materials from energy storage and conversion, catalysis, photocatalysis, adsorption, separation, and sensing to biomedicine, *Chem. Soc. Rev.* 45 (2016) 3479–3563.
- [6] D. Siltamaki, S. Chen, F. Rahmati, J. Lipkowski, A.C. Chen, Synthesis and electrochemical study of CuAu nanodendrites for CO_2 reduction, *J. Electrochem.* 27 (2021) 278–290.
- [7] H. Chen, X. Liang, Y.P. Liu, X. Ai, T. Asefa, X.X. Zou, Active site engineering in porous electrocatalysts, *Adv. Mater.* 32 (2020), 2002435.
- [8] Z. Jiang, Z.P. Li, Z.H. Qin, H.Y. Sun, X.L. Jiao, D.R. Chen, LDH nanocages synthesized with MOF templates and their high performance as supercapacitors, *Nanoscale* 5 (2013) 11770–11775.
- [9] P. He, X.Y. Yu, X.W. Lou, Carbon-incorporated nickel-cobalt mixed metal phosphide nanoboxes with enhanced electrocatalytic activity for oxygen evolution, *Angew. Chem. Int. Ed.* 56 (2017) 3897–3900.
- [10] H. Hu, B.Y. Guan, B.Y. Xia, X.W. Lou, Designed formation of $\text{Co}_3\text{O}_4/\text{NiCo}_2\text{O}_4$ double-shelled nanocages with enhanced pseudocapacitive and electrocatalytic properties, *J. Am. Chem. Soc.* 137 (2015) 5590–5595.
- [11] J. Shao, Z.M. Wan, H.M. Liu, H.Y. Zheng, T. Gao, M. Shen, Q.T. Qu, H.H. Zheng, Metal organic frameworks-derived Co_3O_4 hollow dodecahedrons with controllable interiors as outstanding anodes for Li storage, *J. Mater. Chem. A* 2 (2014) 12194–12200.
- [12] B.W. Zhang, Z.Y. Qi, Z.S. Wu, Y.H. Lui, T.H. Kim, X.H. Tang, L. Zhou, W.Y. Huang, S. Hu, Defect-rich 2D material networks for advanced oxygen evolution catalysts, *ACS Energy Lett.* 4 (2019) 328–336.
- [13] J.D. Chen, F. Zheng, S.J. Zhang, A. Fisher, Y. Zhou, Z.Y. Wang, Y.Y. Li, B.B. Xu, J. T. Li, S.G. Sun, Interfacial interaction between FeOOH and Ni-Fe LDH to modulate the local electronic structure for enhanced OER electrocatalysis, *ACS Catal.* 8 (2018) 11342–11351.
- [14] X.H. Xia, S.F. Xie, M.C. Liu, H.C. Peng, N. Lu, J.G. Wang, M.J. Kim, Y.N. Xia, On the role of surface diffusion in determining the shape or morphology of noble-metal nanocrystals, *P. Natl. Acad. Sci.* 110 (2013) 6669–6673.
- [15] T. Wang, S.L. Zhang, X.B. Yan, M.Q. Lyu, L.Z. Wang, J. Bell, H.X. Wang, 2-methylimidazole-derived Ni-Co layered double hydroxide nanosheets as high rate capability and high energy density storage material in hybrid supercapacitors, *ACS Appl. Mater. Interfaces* 9 (2017) 15510–15524.

- [16] F. Song, X.L. Hu, Ultrathin cobalt-manganese layered double hydroxide is an efficient oxygen evolution catalyst, *J. Am. Chem. Soc.* 136 (2014) 16481–16484.
- [17] H.G. Liao, D. Zherebetsky, H.L. Xin, C. Czarnik, P. Ercius, H. Elmlund, M. Pan, L. W. Wang, H.M. Zheng, Facet development during platinum nanocube growth, *Science* 345 (2014) 916–919.
- [18] H.G. Liao, L.K. Cui, S. Whitlam, H.M. Zheng, Real-Time imaging of Pt₃Fe nanorod growth in solution, *Science* 336 (2012) 1011–1014.
- [19] J.Y. Zhang, G. Li, H.G. Liao, S.G. Sun, Tracking the atomic pathways of Pt₃Ni-Ni (OH)₂ core-shell structures at the gas-liquid interface by in-situ liquid cell TEM, *Sci. China Chem.* 63 (2020) 513–518.
- [20] J.Y. Zhang, S.G. Sun, H.G. Liao, In-situ liquid cell TEM investigation on assembly and symmetry transformation of Pt superlattice, *Sci. China Mater.* 63 (2020) 602–610.
- [21] J.P. Patterson, P. Abellan, M.S. Denny, C. Park, N.D. Browning, S.M. Cohen, J. E. Evans, N.C. Gianneschi, Observing the growth of metal-organic frameworks by in situ liquid cell transmission electron microscopy, *J. Am. Chem. Soc.* 137 (2015) 7322–7328.
- [22] K.M. Vailonis, K. Gnanasekaran, X.B. Powers, N.C. Gianneschi, D.M. Jenkins, Elucidating the growth of metal-organic nanotubes combining isorecticular synthesis with liquid-cell transmission electron microscopy, *J. Am. Chem. Soc.* 141 (2019) 10177–10182.
- [23] J.F. Lyu, X.Y. Gong, S.J. Lee, K. Gnanasekaran, X. Zhang, M.C. Wasson, X.J. Wang, P. Bai, X.H. Guo, N.C. Gianneschi, O.K. Farha, Phase transitions in metal-organic frameworks directly monitored through in situ variable temperature liquid-cell transmission electron microscopy and in situ X-ray diffraction, *J. Am. Chem. Soc.* 142 (2020) 4609–4615.
- [24] W.H. Wang, H.W. Yan, U. Anand, U. Mirsaidov, Visualizing the conversion of metal-organic framework nanoparticles into hollow layered double hydroxide nanocages, *J. Am. Chem. Soc.* 143 (2021) 1854–1862.
- [25] J. Yang, J. Koo, S. Kim, S. Jeon, B.K. Choi, S. Kwon, J. Kim, B.H. Kim, W.C. Lee, W. B. Lee, H. Lee, T. Hyeon, P. Ercius, J. Park, Amorphous-phase-mediated crystallization of ni nanocrystals revealed by high-resolution liquid-phase electron microscopy, *J. Am. Chem. Soc.* 141 (2019) 763–768.
- [26] B.H. Kim, J. Heo, S. Kim, C.F. Reboul, H. Chun, D. Kang, H. Bae, H. Hyun, J. Lim, H. Lee, B. Han, T. Hyeon, A.P. Alivisatos, P. Ercius, H. Elmlund, J. Park, Critical differences in 3D atomic structure of individual ligand-protected nanocrystals in solution, *Science* 368 (2020) 60–67.
- [27] S.H. Yu, Y.H. Jiang, Y. Sun, F. Gao, W.X. Zou, H.G. Liao, L. Dong, Real time imaging of photocatalytic active site formation during H₂ evolution by in-situ TEM, *Appl. Catal. B Environ.* 269 (2020), 118820.
- [28] Y. Hua, X.X. Li, C.Y. Chen, H. Pang, Cobalt based metal-organic frameworks and their derivatives for electrochemical energy conversion and storage, *Chem. Eng. J.* 370 (2019) 37–59.
- [29] B. You, N. Jiang, M.L. Sheng, S. Gul, J. Yano, Y.J. Sun, High-performance overall water splitting electrocatalysts derived from cobalt-based metal-organic frameworks, *Chem. Mater.* 27 (2015) 7636–7642.
- [30] W.H. Lee, H.N. Nong, C.H. Choi, K.H. Chae, Y.J. Hwang, B.K. Min, P. Strasser, H. S. Oh, Carbon-supported IrCoOx nanoparticles as an efficient and stable OER electrocatalyst for practicable CO₂ electrolysis, *Appl. Catal. B Environ.* 269 (2020), 118820.
- [31] W.J. Zhu, L. Zhang, S.H. Liu, A. Li, X.T. Yuan, C.L. Hu, G. Zhang, W.Y. Deng, K. T. Zang, J. Luo, Y.M. Zhu, M. Gu, Z.J. Zhao, J.L. Gong, Enhanced CO₂ electroreduction on neighboring Zn/Co monomers by electronic effect, *Angew. Chem. Int. Ed.* 59 (2020) 12664–12668.
- [32] H. Yang, X. Yu, J. Shao, J. Liao, G. Li, Q. Hu, X. Chai, Q. Zhang, J. Liu, C. He, In situ encapsulated and well dispersed Co₃O₄ nanoparticles as efficient and stable electrocatalysts for high-performance CO₂ reduction, *J. Mater. Chem. A* 8 (2020) 15675–15680.
- [33] F.P. Pan, W. Deng, C. Justiniano, Y. Li, Identification of champion transition metals centers in metal and nitrogen-codoped carbon catalysts for CO₂ reduction, *Appl. Catal. B Environ.* 226 (2018) 463–472.
- [34] C.H. Li, X. Tong, P. Yu, W. Du, J. Wu, H. Rao, Z.M.M. Wang, Carbon dioxide photo/electroreduction with cobalt, *J. Mater. Chem. A* 7 (2019) 16622–16642.
- [35] R. Zhou, N. Han, Y.G. Li, Recent advances in bismuth-based CO₂ reduction electrocatalysts, *J. Electrochem.* 25 (2019) 445–454.
- [36] Y. Cheng, S.Y. Zhao, H.B. Li, S. He, J.P. Veder, B. Johannessen, J.P. Xiao, S.F. Lu, J. Pan, M.F. Chisholm, S.Z. Yang, C. Liu, J.G. Chen, S.P. Jiang, Unsaturated edge-anchored Ni single atoms on porous microwave exfoliated graphene oxide for electrochemical CO₂, *Appl. Catal. B Environ.* 243 (2019) 294–303.
- [37] M. Sartin, W. Chen, F. He, Y.X. Chen, Recent progress in the mechanistic understanding of CO₂ reduction on copper, *J. Electrochem.* 26 (2020) 41–53.
- [38] Y.N. Gong, L. Jiao, Y.Y. Qian, C.Y. Pan, L.R. Zheng, X.C. Cai, B. Liu, S.H. Yu, H. L. Jiang, Regulating the coordination environment of MOF-templated single-atom nickel electrocatalysts for boosting CO₂ reduction, *Angew. Chem. Int. Ed.* 59 (2020) 2705–2709.
- [39] L. Jiao, W.J. Yang, G. Wan, R. Zhang, X.S. Zheng, H. Zhou, S.H. Yu, H.L. Jiang, Single-atom electrocatalysts from multivariate metal-organic frameworks for highly selective reduction of CO₂ at low pressures, *Angew. Chem. Int. Ed.* 59 (2020) 20589–20595.
- [40] Y. Zhang, L. Jiao, W.J. Yang, C.F. Xie, H.L. Jiang, Rational fabrication of low-coordinate single-atom Ni electrocatalysts by MOFs for highly selective CO₂ reduction, *Angew. Chem. Int. Ed.* 60 (2021) 7607–7611.
- [41] L. Jiao, J. Zhu, Y. Zhang, W. Yang, S. Zhou, A. Li, C. Xie, X. Zheng, W. Zhou, S. H. Yu, H.L. Jiang, Non-bonding interaction of neighboring Fe and Ni single-atom pairs on MOF-derived N-doped carbon for enhanced CO₂ electroreduction, *J. Am. Chem. Soc.* 143 (2021) 19417–19424.
- [42] T.J. Woehl, T. Prozorov, The mechanisms for nanoparticle surface diffusion and chain self-assembly determined from real-time nanoscale kinetics in liquid, *J. Phys. Chem. C* 119 (2015) 21261–21269.
- [43] H.M. Zheng, S.A. Claridge, A.M. Minor, A.P. Alivisatos, U. Dahmen, Nanocrystal diffusion in a liquid thin film observed by in situ transmission electron microscopy, *Nano Lett.* 9 (2009) 2460–2465.
- [44] F.M. Ross, *Liquid Cell Electron Microscopy*, Cambridge University Press, New York, 2017, pp. 191–209.
- [45] L.L. Luo, M. Su, P.F. Yan, L.F. Zou, D.K. Schreiber, D.R. Baer, Z.H. Zhu, G.W. Zhou, Y.T. Wang, S.M. Brummer, Z.J. Xu, C.M. Wang, Atomic origins of water-vapour-promoted alloy oxidation, *Nat. Mater.* 17 (2018) 514–518.
- [46] Y. Lin, H. Skaff, T. Emrick, A.D. Dinsmore, T.P. Russell, Nanoparticle assembly and transport at liquid-liquid interfaces, *Science* 299 (2003) 226–229.
- [47] M. Rahimi, T.F. Roberts, J.C. Armas-Perez, X.G. Wang, E. Bokusoglu, N.L. Abbott, J.J. de Pablo, Nanoparticle self-assembly at the interface of liquid crystal droplets, *P. Natl. Acad. Sci.* 112 (2015) 5297–5302.
- [48] X.C. Shen, S. Dai, C.L. Zhang, S.Y. Zhang, S.M. Sharkey, G.W. Graham, X.Q. Pan, Z. M. Peng, In situ atomic-scale observation of the two-dimensional Co(OH)₂ transition at atmospheric pressure, *Chem. Mater.* 29 (2017) 4572–4579.
- [49] G.H. Lin, X. Zhu, U. Anand, Q. Liu, J.Y. Lu, Z. Aabdin, H.B. Su, U. Mirsaidov, Nanodroplet-mediated assembly of platinum nanoparticle rings in solution, *Nano Lett.* 16 (2016) 1092–1096.
- [50] R. Viswanatha, D.D. Sarma, Growth of Nanocrystals In Solution Nanomaterials Chemistry, in: Weinheim, Wiley-VCH Verlag GmbH & Co.KGaA, Weinheim, 2007, pp. 139–170.
- [51] S.R. Becker, P.H. Poole, F.W. Starr, Fractional Stokes-Einstein and Debye-Stokes-Einstein relations in a network-forming liquid, *Phys. Rev. Lett.* 97 (2006), 055901.
- [52] K.K. Wong, C.J. Chen, K. Wei, V.A.L. Roy, S.M. Chathoth, Diffusion of gold nanoparticles in toluene and water as seen by dynamic light scattering, *J. Nanopart. Res.* 17 (2015) 153.
- [53] A. Tuteja, M.E. Mackay, S. Narayanan, S. Asokan, M.S. Wong, Breakdown of the continuum Stokes-Einstein relation for nanoparticle diffusion, *Nano Lett.* 7 (2007) 1276–1281.
- [54] E. Araujo-Lopez, J.S. Lopez-Echeverry, S. Reif-Acherman, The Antoine equation of state: rediscovering the potential of an almost forgotten expression for calculating volumetric properties of pure compounds, *Chem. Eng. Sci.* 177 (2018) 89–109.
- [55] A. Senol, Solvation-based vapour pressure model for (solvent plus salt) systems in conjunction with the Antoine equation, *J. Chem. Thermodyn.* 67 (2013) 28–39.
- [56] Q. Shen, X.F. Huang, J.B. Liu, C.Y. Guo, G.H. Zhao, Biomimetic photoelectrocatalytic conversion of greenhouse gas carbon dioxide: two-electron reduction for efficient formate production, *Appl. Catal. B Environ.* 201 (2017) 70–76.
- [57] Z.Y. Sun, N. Talreja, H.C. Tao, J. Texter, M. Muhler, J. Strunk, J.F. Chen, Catalysis of carbon dioxide photoreduction on nanosheets: fundamentals and challenges, *Angew. Chem. Int. Ed.* 57 (2018) 7610–7627.
- [58] R. Nazir, A. Khalfani, O. Abdelfattah, A. Kumar, M.A.S. Saad, S. Ali, Nanosheet synthesis of mixed Co₃O₄/CuO via combustion method for methanol oxidation and carbon dioxide reduction, *Langmuir* 36 (2020) 12760–12771.
- [59] R. Krishna, Diffusion in porous crystalline materials, *Chem. Soc. Rev.* 41 (2012) 3099–3118.